Chromium-diffusion-induced degradation in metal-supported solid oxide fuel cells with porous stainless-steel supports

Miura, Yohei
Hydrogen Institute for Sustainability (HYDROGENIUS), Kyushu University

Takemiya, Satoshi
Hydrogen Institute for Sustainability (HYDROGENIUS), Kyushu University

Shibata, Yuuki
Hydrogen Institute for Sustainability (HYDROGENIUS), Kyushu University

Cho, Yuki
EV System Laboratory, Nissan Research Center, Nissan Motors Company, Ltd

他

出版情報：Journal of Power Sources. 678, pp.240130-, 2026-06-30. Elsevier
バージョン：

Journal of Power Sources 678 (2026) 240130

Contents lists available at ScienceDirect

Journal of Power Sources

journal homepage: www.elsevier.com/locate/jpowsour

Chromium-diffusion-induced degradation in metal-supported solid oxide fuel cells with porous stainless-steel supports

Yohei Miura [a,b,*], Satoshi Takemiya [a], Yuuki Shibata [a], Yuki Cho [b], Kosuke Hara [b], Takeshi Shiomi [b], Gen Inoue [c], Prabhakar Singh [d], Shunsuke Taniguchi [a], Kazunari Sasaki [a]

[a] Hydrogen Institute for Sustainability (HYDROGENIUS), Kyushu University, Motooka 744, Nishi-ku, Fukuoka, 819-0395, Japan
[b] EV System Laboratory, Nissan Research Center, Nissan Motors Company, Ltd, 1 Natsushima-cho, Yokosuka-shi, Kanagawa, 237-8523, Japan
[c] Department of Chemical Engineering, Faculty of Engineering, Kyushu University, Motooka 744, Nishi-ku, Fukuoka, 819-0395, Japan
[d] Department of Materials Science and Engineering, University of Connecticut, Storrs, CT 06269, United States of America

HIGHLIGHTS

- Ni-Cr formation in anode could degrade hydrogen oxidation reaction activity.
- Breakaway oxidation occurs in fine alloy particles at the anode interface.
- AI-assisted phase segmentation quantifies oxidation of porous stainless steel.
- ASR of porous metal support remains 7.3 mΩ cm^2 after 8400 h.
- Porous stainless steel has a risk of chromium depletion during operation.

ARTICLE INFO

Keywords:
Metal-supported solid oxide fuel cells
Cr diffusion
Steam oxidation
Oxide scale formation
Long-term durability

ABSTRACT

The degradation mechanisms in metal-supported solid oxide fuel cells (MS-SOFCs) are investigated through long-term durability testing and oxidation analysis of porous stainless steel under a humidified hydrogen atmosphere. An MS-SOFC fabricated using 1C44Mo29 steel undergoes a durability test for 8400 h, resulting in a degradation rate of 5.2 %/1000h. Post-test analysis reveals breakaway oxidation of fine alloy particles at the interface between the zirconia-based anode backbone and metal support, along with Ni–Cr formation within the anode, which potentially increases ohmic resistance and hydrogen oxidation polarization resistance. To analyze the correlation between microstructural changes and the electrical resistance of porous stainless steel, a volumetric segmentation scheme is developed using a deep learning model applied to three-dimensional reconstructions from plasma focused ion beam scanning electron microscopy. The results demonstrate that the contribution of metal support oxidation to the overall cell performance is only 7.3 mΩcm^2 even after 8400 h under 50% H_2–50% H_2O, indicating a minimal impact on cell performance; however, Cr depletion in the metal support can cause detrimental degradation.

1. Introduction

Metal-supported solid oxide fuel cells (MS-SOFCs) have garnered attention as efficient systems for converting fuel into electricity [1–5]. Compared to ceramic-supported cells, MS-SOFCs exhibit greater mechanical strength, making them well suited for dynamic operations such as rapid start-up and redox processes [6,7]. Given these advantages, MS-SOFCs are considered promising sources for auxiliary power units in heavy-duty vehicles, as well as for range extenders in electric vehicles, unmanned aerial vehicles, and aircraft [8–12]. In parallel, metal-supported solid oxide electrolyzers are regarded as efficient systems for harnessing energy from intermittent renewable sources such as solar and wind power [13–15]. These devices typically use ferritic stainless steels as metal supports, as their thermal expansion coefficients are compatible with those of the anode and electrolyte components. Although high-temperature oxidation increases the electrical resistance of stainless steel and reduces the mechanical strength of the support, the resulting oxide scale inhibits further degradation [16–18].

* Corresponding author. Hydrogen Institute for Sustainability (HYDROGENIUS), Kyushu University, Motooka 744, Nishi-ku, Fukuoka, 819-0395, Japan.
E-mail address: miura.yohei.825@m.kyushu-u.ac.jp (Y. Miura).

https://doi.org/10.1016/j.jpowsour.2026.240130
Received 24 September 2025; Received in revised form 22 March 2026; Accepted 14 April 2026
Available online 19 April 2026

Powder metallurgy and laser drilling are commonly employed to fabricate metal supports. Specifically, because porous metal supports exhibit better gas diffusion than laser drilling supports, they are more suited for high-power automotive applications. Furthermore, the performance and durability of MS-SOFCs with porous stainless steel supports have been widely studied [1,2,5,14,15,19–22]. For instance, researchers at the Technical University of Denmark developed MS-SOFCs and stacks using a 22Cr tape-cast support and performed durability testing in a humidified hydrogen atmosphere [22]. While degradation rates were reported at both the cell and stack levels, the above studies did not thoroughly examine the individual degradation phenomena contributing to performance loss. Although Cr influences anode degradation [23], the mechanism underlying the deterioration of the infiltrated Ni catalyst remains unclear.

The oxidation behavior of porous stainless steel has been widely investigated in air, where oxide scale growth follows Wagner's law [24–31]. For instance, Reiss et al. modeled the three-dimensional (3D) structural evolution of porous stainless steel assuming that oxide scale growth follows Wagner's law, further predicting its effect on electrical resistance [24]. Koszelow et al. quantitatively analyzed how oxide scale growth varies with pre-oxidation in porous Fe22Cr using 3D X-ray tomography reconstructions [25]. Ibrahim et al. combined X-ray tomography with generative-adversarial-network-derived 3D models and weight gain measurements to analyze Cr content [31]. However, compared to air, degradation phenomena in the anode atmosphere are more difficult to interpret. Microstructural changes in the oxide scale are assessed using cross-sectional scanning electron microscopy (SEM) images, while thickness variation on the alloy surface is measured using the Otsu algorithm, which detects grayscale differences between objects. Nonetheless, the ambiguous contrast between the alloy and oxide scale makes it necessary to set binary segmentation thresholds for each 2D slice.

Recently, deep learning models have been extensively applied for accurate volumetric phase segmentations of electrode composites in solid oxide cells [32–34]. Despite these advances, no studies have yet examined oxidation phenomena in porous stainless steel using deep learning-based volumetric segmentation, especially under hydrogen-rich atmospheres relevant to solid oxide fuel cells (SOFCs). While previous research has primarily focused on oxide growth in air or microstructural analysis, the integration of deep learning segmentation techniques to directly analyze oxidation in porous stainless steel during long-term hydrogen exposure is a novel approach that can provide deeper insights into degradation mechanisms.

In response, this study investigates the correlation between resistance evolution and microstructural degradation in MS-SOFCs through an 8400-h durability test. Subsequently, the relationship between the oxidation of porous stainless steel and the rise in area-specific resistance (ASR) under highly humidified hydrogen exposure is quantitatively examined using volumetric phase segmentation with a deep learning model. The microstructure and ASR are also predicted using the parabolic oxidation rate constant derived from weight gain measurements. Based on these results, the dominant degradation factors in MS-SOFCs with porous stainless steel supports during long-term operation are identified.

2. Experimental

2.1. Cell fabrication

A metal-supported button cell was fabricated using 1C44Mo29 (21Cr, Sandvik). The diameters of the metal support and the cathode are 30 mm and 9 mm, respectively. Table 1 specifies the composition of 21Cr, exhibiting a mean particle diameter (D_{50}) of approximately 20 μm. The materials and thicknesses of each layer in the button cell are summarized in Table 2. To employ 21Cr as the metal support, fine 21Cr powder (D_{50}: ~5 μm) mixed with Sc- and Y-stabilized ZrO_2 (ScYSZ; Daiichi Kigenso, Japan) was used as a bonding layer, which was inserted between the metal support and anode to reduce interfacial resistance. Meanwhile, ScYSZ mixed with a pore former was used as the anode backbone, while pure ScYSZ was used as the electrolyte. A 0.8-μm polymethyl methacrylate was used as the pore former, and the weight was adjusted so that the volume ratio of the pore former to ScYSZ was 2:5, to increase the specific surface area of the anode reaction. Each material was combined with a butyral-based organic binder, cast onto Mylar tape, and laminated. The laminate was debinded in air and sintered at 1250 °C for 1 h in a 10% H_2–90% Ar atmosphere. Following sintering, a 1 μm gadolinia-doped ceria (GDC) layer was deposited onto the electrolyte surface via physical vapor deposition, followed by wet infiltration of an Ni/GDC catalyst into the anode backbone. Infiltration solutions were prepared by mixing nitrates of Ni, Gd, and Ce with Triton™ X-100 (Sigma Aldrich, USA) and ultrapure water. The anode backbone was treated with this solution, dried, and calcined at 800 °C for 30 min in air. This was followed by two additional infiltration and calcination steps, each performed at 650 °C for 30 min in air. Finally, a lanthanum strontium cobaltite (LSC, DOWA Holdings, Japan) cathode was applied to the GDC barrier layer via screen printing.

2.2. Electrochemical performance testing

The metal-supported button cell was mounted in an alumina tube for performance evaluation. The cell edges were sealed with Pyrex® glass, and Pt meshes with wires were positioned on the cathode and anode as current collectors. A detailed description of the setup is available in Ref. [3]. After the cell was mounted in the alumina tube, the temperature was raised from room temperature to 800 °C and maintained for 6 h to sinter the cathode. Air was supplied to the cathode, while the anode was exposed to a mixture of 78% H_2–16% N_2-6% H_2O. This composition simulates the reformate gas produced by ethanol steam reforming in an external reformer; both gases were delivered at a total flow rate of 100 sccm. The current–voltage (I–V) curve and impedance were measured after *in situ* cathode sintering. Electrochemical impedance spectroscopy (EIS) was performed using a frequency response analyzer (VERSASTAT4-400, Princeton Applied Research) under an open-circuit voltage (OCV). The spectra were collected over a frequency range from 3.98 Hz to 100,000 Hz.

Table 2
Material and thickness details of the metal-supported button cell.

Layer	Material	Thickness [μm]
Cathode	LSC	30–40
Diffusion barrier layer	GDC	1
Electrolyte	ScYSZ	8
Anode	Ni/GDC-infiltrated ScYSZ	4
Anode bonding layer	21Cr(1C44Mo29)/ScYSZ	40
Metal support	21Cr(1C44Mo29)	300

Table 1
Chemical composition of the 21Cr alloy.

	Fe	Cr	Ni	Mn	Mo	Nb	Si	Al	C	O	N	S	P
1C44Mo29	Bal.	21.0	0.03	0.11	0.94	0.43	0.05	0.02	0.01	0.16	0.07	0.01	0.01

2.3. Oxidation and electrical resistance measurement under humidified hydrogen conditions

Approximately 200-μm-thick porous stainless-steel plates were fabricated by sintering 21Cr powder at 1250 °C for 1 h in a 10% H_2–90% Ar atmosphere. The plates were cut into 10 mm × 10 mm squares for weight gain measurements and electrical resistance evaluation. The specimens were then pre-oxidized at 800 °C for 10 h in ambient air to enable oxide scale formation on the alloy surface.

Cleaned and degreased specimens were exposed to a 50% H_2–50% H_2O gas mixture at 600 °C, simulating the realistic operating condition. The porous specimens were placed in a quartz tube and heated in an electric furnace. Hydrogen and nitrogen gases, subjected to water bubbling, were introduced into the tube. The bubbling temperature and flow rates were controlled using mass flow controllers to adjust the gas composition. The total flow rate was maintained at 100 sccm. After the designated exposure period, the furnace was cooled to room temperature, and weight gain was measured using an analytical balance with 0.01 mg precision.

The electrical resistance of the porous stainless steel specimens was evaluated in the through-plane direction (Fig. S1) using an impedance analyzer (HIOKI IM-3570). This resistance, governed by the oxide scale's thickness and chemistry and the alloy's 3D structure, was measured using pre-oxidized samples. It was monitored for 650 h at 600 °C under 50% H_2–50% H_2O, and variations were compared accordingly. Pt foils with welded Pt wires were placed on both sides of the 10 mm × 10 mm oxidized test pieces, and resistance measurements were conducted under compression applied through an alumina tube. ASRs were calculated by multiplying the through-plane resistance by the current-collecting area.

2.4. Characterization

The cross-sectional microstructure of the button cell was examined using field-emission SEM (FE-SEM; Carl Zeiss Ultra55) coupled with energy-dispersive X-ray spectroscopy (EDS; HITACHI SU-8230). Nanoscale structural changes in the oxide scale and anode catalyst of the MS-SOFC were investigated using scanning transmission electron microscopy (STEM) coupled with EDS. For microscopic analysis, porous stainless steel and button cells were embedded in organic resin, polished to reveal the cross section, and thinned using a focused ion beam (FIB) to permit electron beam penetration. Talos F200X and Super-X (FEI) were used to analyze the oxide scale microstructure of porous stainless steel, whereas ARM200F and JED-2300T (JEOL) were employed to examine the microstructure of the infiltrated anode catalyst in the metal-supported cell. Plasma focused ion beam SEM (FIB-SEM) was conducted using Helios 5 Hydra (FEI) to analyze the porous metal support, with Xe ion milling enabling large-area processing. A slice interval of 250 nm was used, and 500 slices were acquired to generate a 125 μm box volume. The acceleration voltage was set to 2 kV, and backscattered electron images were acquired for each sliced cross section.

3. Results and discussion

3.1. Initial performance and long-term durability testing

3.1.1. Initial performance

Fig. 1(a) presents the I–V curves of the button cell at 600 °C and 700 °C under 78% H_2–16% N_2–6% H_2O. The power densities are 0.283 Wcm^{-2} at 600 °C, 0.7 V and 0.957 Wcm^{-2} at 700 °C, 0.7 V. Fig. 1(b) presents the ohmic and polarization resistances. Notably, the ohmic resistances, defined as the intercept on the real axis, are 0.441 Ωcm^2 at 600 °C and 0.166 Ωcm^2 at 700 °C, while the corresponding polarization resistances are 0.299 Ωcm^2 and 0.194 Ωcm^2, respectively.

3.1.2. Long-term durability over 8400 h

The target operational lifetime of SOFCs in vehicle applications is approximately 10000 h or longer [35]. In this study, we conducted a durability test lasting 8400 h. Fig. 2(a) illustrates the variation in current density at 0.85 V, 600 °C over the test period. The temperature for the durability test was set at 600 °C, which is suitable for rapid startup in mobile applications at low temperature. Additionally, the cell voltage was set to 0.85 V, corresponding to the rated cell voltage of the system. The degradation rates were 9.2 %/1000 h for 0–640 h, 5.4 %/1000 h for 640–3750 h, and 5.2 %/1000 h for 3750–8400 h. Based on Fig. 2(a), delamination, which would cause discontinuous changes in long-term operation, did not occur. Further, to assess changes in ohmic and polarization resistances during the test, I–V and EIS measurements were conducted at 0, 640, and 8400 h. The I–V curve (Fig. 2(b)) indicated that the OCV remains stable at 1.080 V over 0–8400 h, suggesting no notable increase in gas leakage. Also, in the I–V curve after the durability test (Fig. 2(b)), there was no remarkable drop in cell voltage at high current densities, indicating that pore blockage, which would limit anode gas supply, also did not occur. From the EIS results obtained in the durability test in Fig. 2(c) and (d), electrode resistances were deconvoluted into individual processes using the complex non-linear least squares (CNLS) fitting on ZView. The EIS measurements were performed from 3.98 Hz to 100,000 Hz, and fitting was carried out with an equivalent circuit composed of inductance (L), ohmic resistance (Rs), ionic transport (R1), oxygen electrode reaction (R2), cathode kinetics (R3), and anode kinetics (R4) (Fig. S2(a) and (b)). In the fitting, the inductance of the

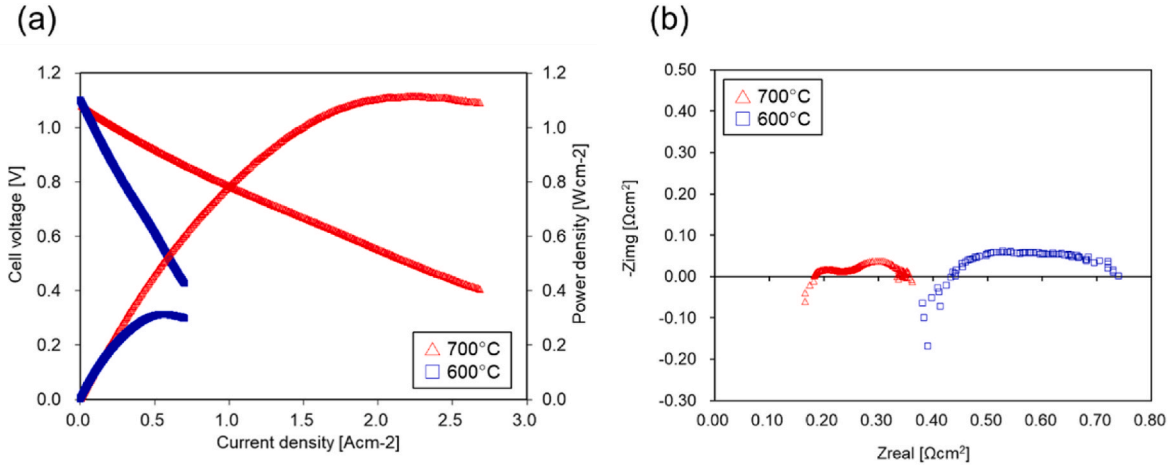

Fig. 1. (a) I–V curve and (b) Cole–Cole plot of the metal-supported button cell. Fuel composition: 78% H_2–16% N_2–6% H_2O.

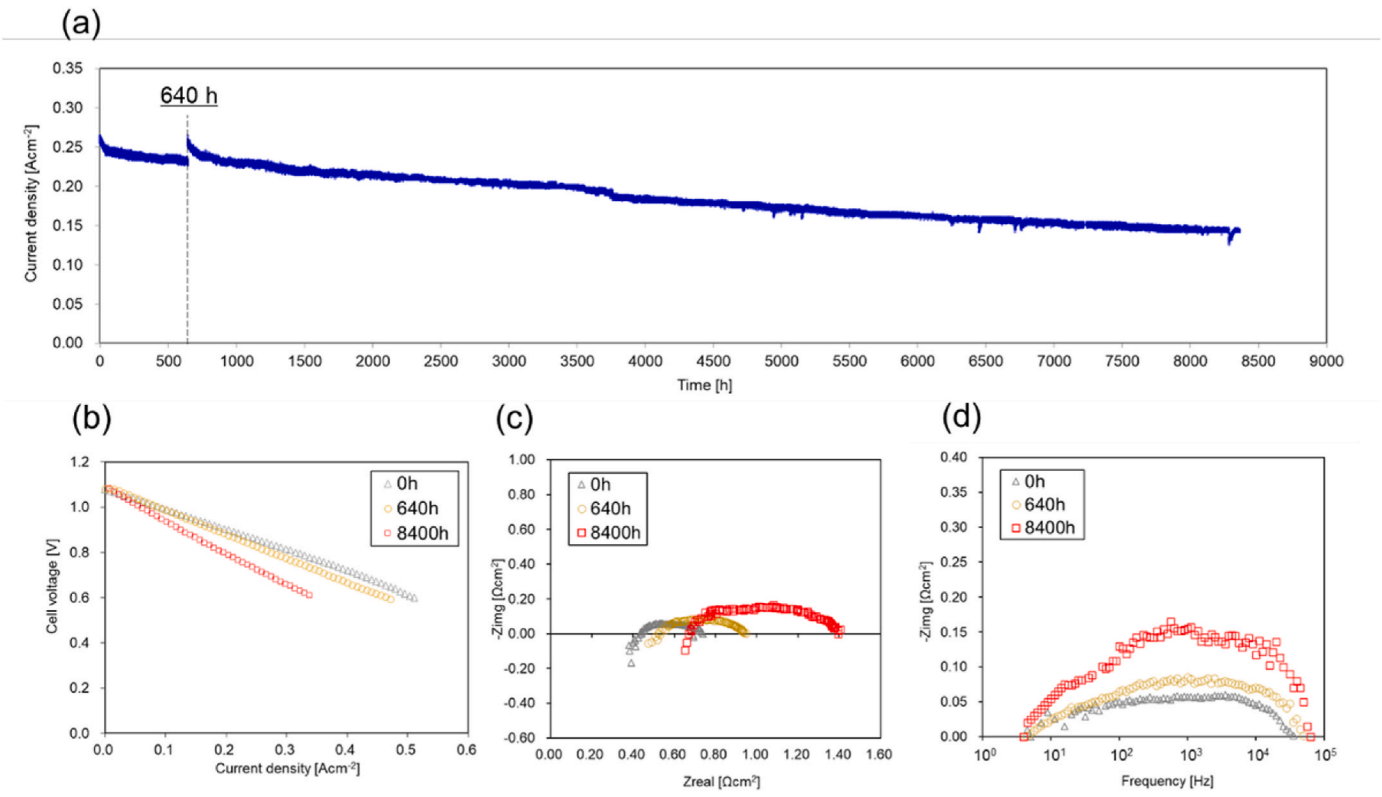

Fig. 2. (a) Current density variation during the durability test at 600 °C and 0.85 V under 78% H_2–16% N_2–6% H_2O. (b) I–V curves, (c) Cole–Cole plots, and (d) Bode plots evaluated during the test. The EIS spectra were collected over a frequency range from 3.98 Hz to 100,000 Hz.

connecting wires was accounted when determining the ohmic resistance (Fig. S2(c)). Based on previous research [36], the characteristic peak frequencies of the semicircles for each resistive element in the equivalent circuit were set to R1 = 8500 Hz, R2 = 1600 Hz, R3 = 300 Hz, and R4 = 50 Hz, respectively. The changes of R2, R3, and R4 are shown in Fig. S2(d). R2 and R3, which constitute the cathode, increase over 8400 h, whereas R4, which constitutes the anode, increases rapidly over 640 h. These results suggest that anode degradation occurs primarily in the initial phase, while cathode degradation may progress gradually over a longer period.

3.1.3. Degradation mechanism

The sample microstructure was analyzed using FE-SEM after the durability test. No notable changes were observed in either the electrolyte or the metal support. The oxide scale formed on the metal support is expected to suppress steam oxidation of the alloy. However, severe oxidation was observed in fine alloy particles within the anode bonding layer (Fig. 3). Smaller alloy particles generally exhibit lower corrosion resistance owing to inadequate Cr content to form Cr_2O_3 scales on their surfaces. Before steam oxidation (Fig. 3(a)), a ~0.5 μm Cr_2O_3 scale formed at the ScYSZ/21Cr interface. After the durability test (Fig. 3 (b)), breakaway oxidation occurred, suggesting that Cr diffused into the ScYSZ phase and the Cr concentration in the alloy particles dropped below the threshold. Because iron oxide and Cr_2O_3 exhibit low electronic conductivity [37,38], this breakaway oxidation may have contributed to the increased ohmic resistance. The ohmic resistance measured before and after the durability test showed a substantial increase of 0.171 Ωcm^2 (i.e., 0.572 minus 0.401 Ωcm^2) over 8400 h from Fig. S2(c). Since the contact among the cathode, anode, and Pt current collector is maintained with a constant load, and its contribution is minimal, the initial ohmic resistance mainly arises from zirconia phase transformation and oxidation of the bonding layer. Here, the contributions of each factor to the initial ohmic resistance are calculated. The electrolyte used in this study has the same fabrication conditions as in Ref. [39]. Because it was sintered at low temperature, it contained many grain boundaries, and its conductivity is approximately 0.3 times that of an ideal dense microstructure. According to previous study [40], the total conductivity of ScSZ is not sensitive to pO_2. Therefore, it was assumed that the total conductivity in the thickness direction of the electrolyte is constant and based on the ionic conductivity and thickness of ScSZ, the ohmic resistance of the electrolyte was calculated to be 0.133 Ωcm^2. According to previous research [41], the conductivity of ScSZ decreases by approximately 1.1–4.1 %/1000h. As a result, an increase in resistance of 0.014–0.070 Ωcm^2 is expected in the electrolyte layer after 8400 h. As shown in Fig. S3(a), stainless alloy particles in the bonding layer are present at intervals of about 20 μm. After 8400 h, Cr_2O_3 scale (red arrows) is grown between the stainless alloy and ScYSZ, or the breakaway oxidation involving the formation of FeOx (white arrows) occurs. The bonding layer is composed of stainless alloy particles, with an average particle size of 5 μm. Since stainless alloy have high electric conductivity, the electron passes through metal oxide, Cr_2O_3 or FeOx in the bonding layer as shown in Fig. S3(b). The increase of ohmic resistance R_{total} [Ωcm^2] can be calculated by the following Equations (1) and (2):

$$R_{MO} = \frac{t}{\sigma \times S}, \tag{1}$$

$$\frac{1}{R_{total}} = \frac{1}{R_{FeOx}} + \frac{1}{R_{Cr2O3}}, \tag{2}$$

where t is the thickness of metal oxide, σ is the conductivity of the metal oxide, and S is the total area obtained by summing the areas of all particles located on the active area of the button cell. Based on the SEM images, it is assumed that two-fifths of the alloy particles have been entirely transformed into 5-μm FeOx particles, and three-fifths consist of alloy particles newly covered by approximately 1-μm Cr_2O_3. The

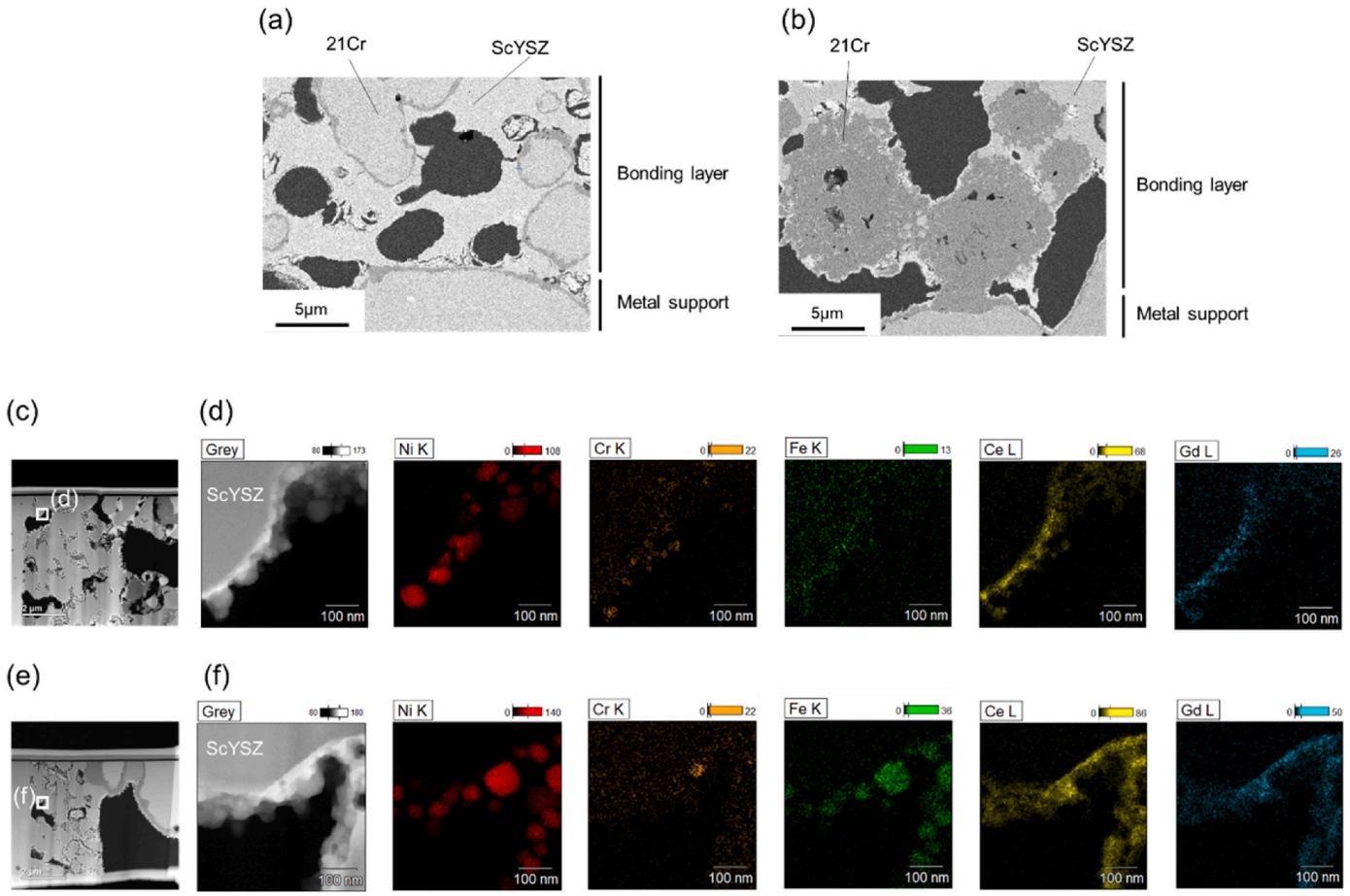

Fig. 3. Cross-sectional FE-SEM images of the bonding layer/metal support interface: (a) before and (b) after the 8400 h durability test. STEM–EDS mappings near the anode/electrolyte interface: (c-d) before and (e-f) after the 8400 h durability test.

calculated resistance is approximately 0.138 Ωcm^2. Thus, the increase in ohmic resistance observed in the durability test (0.171 Ωcm^2) can be explained by the increase in electrolyte resistance and the increased resistance of the bonding layer. In the active area, the areas occupied by Cr_2O_3 and FeOx are only 3% and 2%, respectively. Because the current is concentrated in narrow regions, the resistance should increase.

Fig S4(a-c) shows the quantitative EDS results of Cr content of the bonding layer, anode scaffold, and electrolyte before and after the durability test. Compared with before durability test, the Cr content of the stainless-steel particles decreased after 8400 h. The results of line scans across the quantitative analysis region are shown in Fig. S4(d). After the durability test, Cr was found to have diffused into the anode scaffold and the electrolyte. The Cr concentrations in the scaffold and electrolyte were fitted using the diffusion equation as follows:

$$c(x,t) = \frac{M}{\sqrt{4\pi Dt}} \exp\left(-\frac{x^2}{4Dt}\right), \tag{3}$$

where D is the diffusion coefficient, M is the solute amount, and t is time. The fitting results suggest that Cr is undergoing solid-state diffusion within the ScYSZ of the anode scaffold and electrolyte, rather than vapor-phase diffusion.

The cathode's elemental distribution before and after the durability test was analyzed using SEM–EDS (Fig. S5). Sr segregation was observed after the test, suggesting degradation in oxygen reduction kinetics [42]. TEM analysis was performed to examine changes in the anode catalyst. Additionally, an average field of view was extracted from the low-magnification observations (Fig. 3(c–e)) and used for EDS analysis. At the initial stage (Fig. 3(d)), Gd and Ce were distributed across the ScYSZ backbone surface, and Ni nanoparticles measuring 30–100 nm precipitated. After the durability test (Fig. 3(f)), no notable changes were observed in the size or distribution of the Ni particles, although the specific surface area of the Ni particles has decreased slightly. However, Cr and Fe were detected in the Ni particles; these elements diffused from the bonding layer and formed compounds with Ni. Cr oxide precipitated and diffused from the bonding layer and may have suppressed hydrogen oxidation activity, leading to increased polarization resistance [43]. TEM observation was conducted on only a single cross-section in this study. To analyze particle coarsening and changes in specific surface area in detail, a more quantitative evaluation—such as counting the size and number of particles from multiple cross-sections—is necessary. In this study, the observed increase in polarization resistance primarily originated from Sr segregation in the cathode and Cr oxide precipitation in the anode. Notably, analyzing the polarization sensitivity to oxygen and hydrogen concentrations before and after durability testing enables quantitative assessment of cathode and anode degradation. Because the anode active and bonding layers are adjacent, Fe or Cr can easily diffuse from the bonding layer alloy to the anode catalyst. Removing fine alloy particles from the bonding layer helps mitigate this degradation. As the bonding layer must maintain electronic conductivity, electronically conductive perovskite oxides [44] could serve as alternatives. However, Cr may still diffuse from both the bonding layer and the metal support. During power generation in humidified hydrogen, the Cr vapor pressure remains low regardless of water vapor concentration [45], so solid-state diffusion should be the dominant pathway. During the cell fabrication process, Cr diffuses from the bonding layer into the anode backbone at 1250 °C during co-sintering under a reducing atmosphere, and Cr evaporation occurs when the cell is exposed to air during infiltration at

800 °C and 650 °C. Therefore, Cr is observed from Ni particles even in the initial stages of the durability test. Furthermore, during long-term operation, Ni is poisoned by Cr through solid-state diffusion from the bonding layer into the anode backbone. Incorporating a thin and dense GDC barrier layer between the metal support and bonding layer could effectively limit Cr diffusion from the metal support [46].

To further evaluate the impact of individual degradation phenomena, degradation rates were compared with those reported by other groups studying MS-SOFCs with porous stainless-steel supports at Lawrence Berkeley National Laboratory (LBNL) and the Technical University of Denmark (DTU) [5,22,47,48]. While researchers at LBNL and DTU have recently concentrated on improving solid oxide electrolysis cell durability [14,15,49,50], the present study focuses on fuel cell operation, given the occurrence of Ni percolation during electrolysis [51]. The cell configurations, features, and operating conditions of each system are summarized in Table 3. Compared to the other studies listed in Table 3, the H_2 concentration in our study is lower, and the operating temperature is also reduced. Regarding the H_2 concentration, since the partial pressure of oxygen is significantly lower than the thermodynamic oxidation potential of Ni catalysts and stainless steel, their contribution to degradation is likely minimal. Concerning the temperature, operating at a lower temperature compared to other studies can suppress catalyst coarsening and Cr diffusion [5], but nevertheless, the degradation rate remains higher. This may be due to the acceleration of degradation caused by the insertion of the bonding layer. Notably, at LBNL, the use of a cathode-side metal support and cathode infiltration with praseodymium oxide (PrOx) resulted in substantially higher degradation rates than those observed in conventional MS-SOFCs. Accordingly, oxidation of the cathode-side support, along with catalyst coarsening and degradation, was likely the dominant degradation mechanism of the cells tested at LBNL [5,52]. Further, in contrast to the cells at DTU, the present configuration incorporates a bonding layer between the metal support and anode. When breakaway oxidation occurs within this layer, it not only increases ohmic resistance but also obstructs the vertical flow of current, thereby reducing the effective active area. These effects likely contribute to the higher degradation rate observed in our cell compared with the DTU design. Although the bonding layer can improve ohmic resistance, it may compromise long-term durability. Thus, avoiding the placement of fine stainless-steel particles near the anode backbone and metal support interface may improve long-term performance.

3.2. Quantification of steam oxidation effects in metal supports

Section 3.1 focused on the degradation phenomena of the button cell; however, understanding the oxidation behavior of porous stainless steel, which is governed by its metal support, is also essential. Unlike the low-humidity conditions of our 8400 h durability test, the metal support may encounter highly humidified reducing atmospheres during reforming gas exposure or high fuel utilization on the anode side, both of which can accelerate oxidation. To address this, the weight gain and morphological changes of porous stainless steel under humidified hydrogen exposure were analyzed. Subsequently, the effect on long-term durability was evaluated by quantitatively correlating the electrical resistance with microstructural changes in the porous stainless steel, including oxide scale formation.

3.2.1. Weight gain under steam oxidation and microstructural changes in the oxide scale

Fig. 4 presents the weight gain of as-sintered and pre-oxidized alloy samples exposed to either 50% H_2–50% H_2O or 78% H_2–16% N_2–6% H_2O at 600 °C for 650 h. Notably, 78% H_2–16% N_2–6% H_2O simulates the gas composition used in the durability test described in Section 3.1. Here, weight gain is defined as in Equation (4).

$$\Delta m = 100 \times \frac{m - m_0}{m_0}, \tag{4}$$

where m_0 is the initial weight before oxidation. As illustrated in Fig. 4 (a), a notable weight increase is observed for the sample without pre-oxidation after the initial 125 h, indicating that the surface oxide transforms into a faster-growing multi-constituent scale incorporating intrinsic oxide defects, iron oxides, Cr_2O_3, and MnO_x. In contrast, the lower weight change observed for the pre-oxidized sample is attributed to the formation of an initial oxide barrier resisting further growth. This behavior is different from that of samples without pre-oxidation, which develop a faster-growing oxide during exposure to the steam-containing H_2–H_2O atmosphere (Fig. 4 (b)). Compared to 50% H_2O, the weight gain observed with 6% H_2O is considerably smaller, consistent with the absence of substantial metal support degradation after the durability test. The following sections detail microstructural and electrical resistance changes under 50% H_2–50% H_2O.

3.2.2. Analysis of steam oxidation and ASR in porous stainless steel using volumetric segmentation

For samples before and after steam oxidation, the oxide scale thickness and ASR were calculated using the analytical flow illustrated in Fig. 5. The workflow, implemented using GeoDict [53], included 3D reconstruction, volumetric phase segmentation with a 3D U-Net, Cr_2O_3 thickness analysis, and conductivity calculation for porous stainless steel as follows.

3.2.2.1. 3D reconstruction. The acquired 2D image data were stacked to

Table 3
Comparison of degradation rates with other MS-SOFCs.

		Nissan	LBNL (2019)	DTU (2011)	DTU (2013)	DTU (2020)
Cell concept		Conventional	Symmetric	Conventional	Conventional	Conventional
Configuration		Button cell (0.6 cm^2)	Button cell (1 cm^2)	Button cell (0.5 cm^2)	Large cell (16 cm^2)	Large cell (16 cm^2)
Cell structure	Cathode	LSC	PrOx-infiltrated ScYSZ	LSC	LSC	LSC
	Electrolyte	ScYSZ	ScSZ	ScYSZ	ScYSZ	ScYSZ
	Anode	Ni/GDC-infiltrated ScYSZ	Ni/CGO-infiltrated ScYSZ	Ni/CGO-infiltrated 70 vol% STN99/30 vol% FeCr	Ni/CGO-infiltrated FeCr-YSZ	Ni/CGO-infiltrated FeCr-LSFNT
	Bonding layer	1C44Mo29 /ScYSZ	-	-	-	-
	Metal support	1C44Mo29	P434L	FeCr	FeCr	Fe22Cr
Operating condition	Temperature [°C]	600	700	650	650	650
	Anode gas composition	$H_2/N_2/H_2O$ = 78/16/6 [%]	H_2/H_2O = 97/3 [%]	H_2/H_2O = 96/4 [%]	H_2/H_2O = 96/4 [%]	H_2/H_2O = 80/20 [%]
	Current density or cell voltage	0.85 V (const.)	0.7 V (const.)	0.25 Acm^{-2} (const.)	0.25Acm^{-2} (const.)	0.25A/cm^{-2} (const.)
Degradation rate [%/kh^{-1}]		5.4	39	9	1.1	6
Ref.		-	[5]	[47]	[48]	[22]

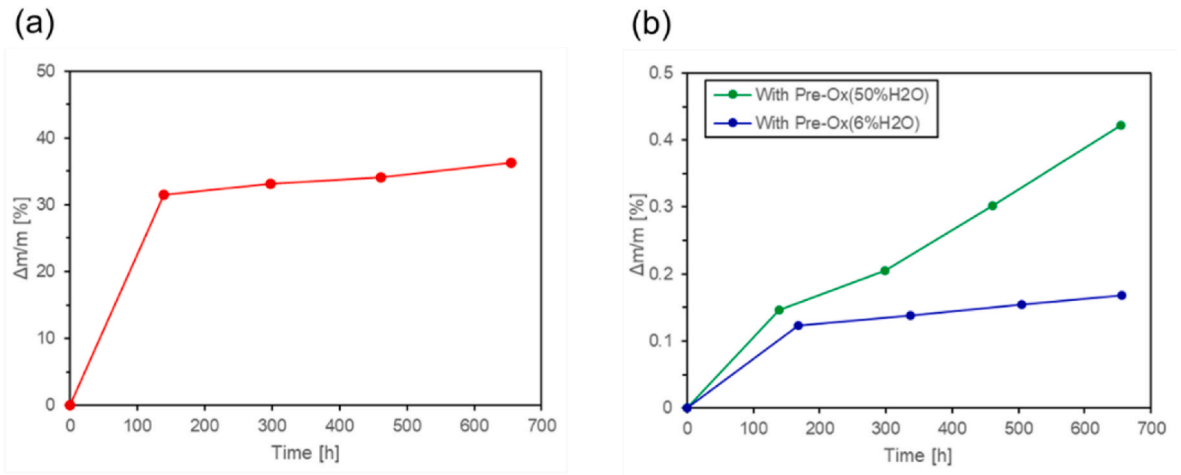

Fig. 4. (a) Weight gain without pre-oxidation at 600 °C under 50% H_2–50% H_2O; (b) weight gain with pre-oxidation under either 50% H_2–50% H_2O or 78% H_2–16% N_2–6% H_2O.

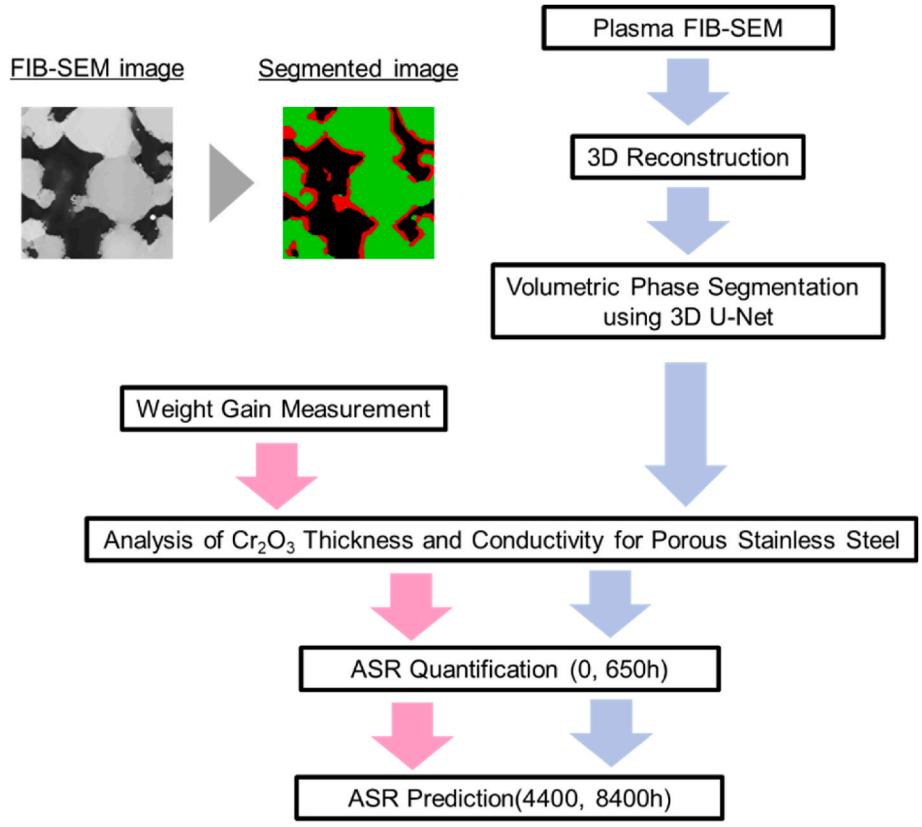

Fig. 5. Analytical workflow used to quantify and predict the ASR of porous stainless steel via volumetric phase segmentation.

generate volume data measuring 125 μm in the x, y, and z directions. During this process, curtain-like patterns appeared on each slice cross-section due to FIB-SEM milling and were removed using image filters.

3.2.2.2. Volumetric phase segmentation using 3D U-Net. In this study, annotations were performed on one cross-section from each of the X, Y, and Z planes of the reconstructed 3D stack because training did not converge when more than two cross-sections were used. One cross-section is composed of 1251 by 981 pixels, and annotations were made on every pixel across the entire surface, not just parts of it. The labels were categorized into three classes: oxide scale, alloy, and pore. Sparse annotation data were used to train a pre-configured 3D U-Net model on GeoDict. Notably, 3D U-Net is a deep-learning-based segmentation method tailored for processing volume data [54]. During training, the model learned the features of pore, alloy, and oxide scale, enabling it to classify each voxel into one of these three classes. After training, voxels in the volume data were segmented accordingly. During segmentation, the 3D U-Net model accurately binarized pore, alloy, and oxide scale by incorporating contextual information between slices. Three annotated images each in the XYZ directions were made for validation, and the accuracy of volumetric segmentation was evaluated using the intersection over union (IoU) and dice similarity coefficient (DSC) [55]. The DSC emphasizes overlapping regions and is used to evaluate overlap in fine-scale regions. Each class (pore, alloy, and oxide

scale) was assigned specific RGB values in both the ground-truth and segmented images. Pixels with these RGB values were designated as ROIs, and the overlap of ROIs between images was determined. This calculation was performed using a custom-coded MATLAB program. For the alloy and pore classes, both metrics exceed 0.9. IoU values above 0.9 are typically considered indicative of high segmentation accuracy [56]. Despite the thin morphology and low volume fraction of the oxide scale, the model achieves DSC values greater than 0.8. Müller previously reported that comparable DSC values are achieved when segmenting binder phases in lithium-ion batteries [57]. Based on this precedent, a DSC of 0.8 is interpreted as indicative of high segmentation accuracy. These results confirm that the segmentation model employed in this workflow provides sufficient fidelity to enable further microstructural analysis and electrical conductivity calculations.

3.2.2.3. Cr_2O_3 thickness analysis and conductivity calculation for porous stainless steel. Based on the segmented image stack, the volumes of each class (oxide scale, alloy, and pore), along with the two-layer interfaces (oxide scale/alloy and pore/oxide scale), were computed using the MatDict module in GeoDict. The oxide scale thickness, L_o, was calculated as follows:

$$L_o = \frac{V_o}{0.5 \times (S_{po} + S_{oa})}, \tag{5}$$

where V_o is the volume of the oxide scale, S_{po} is the interface area between the pore and oxide scale (cm^2), and S_{oa} is the interface area between the oxide scale and alloy. The two-layer interface was estimated by counting voxels along the boundary surfaces and applying diagonal weighting to reflect the actual physical surface area. TEM was conducted to investigate the microstructure of the oxide scale and the surrounding elemental distribution. High-angle annular dark-field STEM images and EDS maps of 21Cr are displayed in Fig. 6(a–c). Prior to steam oxidation, an Mn–Cr spinel oxide formed on the outer layer, while Cr_2O_3 developed beneath it. The thickness of the Mn–Cr spinel oxide was fixed at 450 nm, as this layer, once formed during pre-oxidation, does not permit further Mn diffusion due to the limited Mn content in the alloy. Consequently, the Mn–Cr spinel oxide layer thickness remained unchanged before and after steam oxidation. Finally, the Cr_2O_3 thickness was obtained by subtracting the fixed Mn–Cr spinel oxide thickness from the total oxide scale thickness derived from image analysis.

The thickness of Cr_2O_3 after pre-oxidation (t_{po}) and steam oxidation (t_{so}) was calculated using Equations (6)–(8), based on weight gain measurements.

$$\Delta wt_{MC} = t_{MC} \times S \times d_{MC}, \tag{6}$$

$$t_{po} = \frac{(\Delta wt_{po} - \Delta wt_{MC})}{d_{Cr} \times S}, \tag{7}$$

$$t_{so} = \frac{\Delta wt}{d_{Cr} \times S}, \tag{8}$$

where t_{MC} denotes the thickness of the Mn–Cr spinel oxide; S is the surface area of porous stainless steel measured using the Brunauer–Emmett–Teller (BET) method; d_{MC} and d_{Cr} represent the densities of the Mn–Cr spinel oxide and Cr_2O_3, respectively. The values of d_{MC} and d_{Cr} were sourced from Refs. [58] and [59]. Because the Cr_2O_3 thickness derived from volumetric segmentation differed from that determined through weight gain, both values were used in ASR calculations. Based

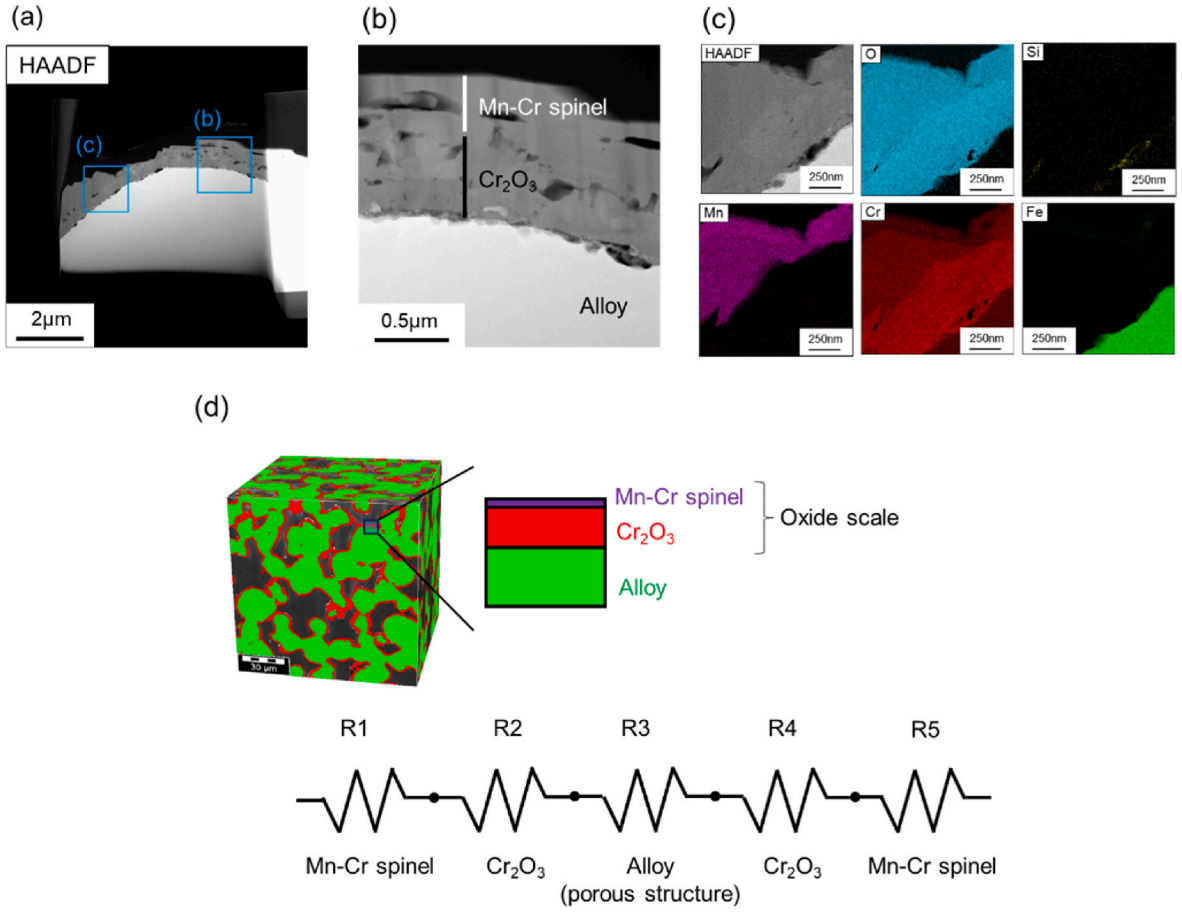

Fig. 6. (a, b) STEM images and (c) EDS maps of 21Cr after pre-oxidation at 800 °C for 10 h. (d) Equivalent circuit model for calculating the ASR of porous stainless steel before and after steam oxidation at 600 °C under 50% H_2–50% H_2O for 650 h.

on the segmented image, the volume resistivity of the porous alloy was computed using the ConductDict module in GeoDict.

3.2.2.4. ASR quantification. Fig. 6(d) presents an equivalent circuit model representing the electrical resistance along the thickness direction of porous stainless steel. Based on the TEM observation, the 1C44Mo29 alloy comprises three layers—Mn–Cr spinel oxide, Cr_2O_3, and the underlying alloy—formed during pre-oxidation. In the model, Mn–Cr spinel oxide corresponds to R1 and R5, Cr_2O_3 corresponds to R2 and R4, and the porous alloy corresponds to R3. As electrons travel along the thickness, they traverse the Mn–Cr spinel oxide and Cr_2O_3 layers, enter the porous alloy, and continue through the Cr_2O_3 and Mn–Cr spinel oxide layers on the opposite side. Accordingly, a series equivalent circuit model comprising five resistance components is constructed. Each resistance component is quantified using its respective thickness and conductivity to evaluate the ASR. Conductivity values for the Mn–Cr spinel oxide [60] and Cr_2O_3 [61] are adopted from previous studies.

Table 4 summarizes the thickness and conductivity of each resistance component used in the calculation of ASR. The Cr_2O_3 thickness by segmentation closely aligned with those obtained through gravimetric analysis. In the values obtained through image segmentation, the Cr_2O_3 thickness increased from 0.51 μm to 0.80 μm after 650 h. Compared to the resistance of Mn-Cr spinel oxide (R1, R5) and Cr_2O_3 (R2, R4), the ASR of stainless steel (R3) was significantly smaller. Although the tortuosity of alloy R3 increased from 1.12 to 1.22 after 650 h, its conductivity is 10^4–10^5 orders of magnitude higher than that of the oxide scale, resulting in a negligible contribution. Because the thickness of the Mn–Cr spinel oxide remains unchanged, the increase in resistance is primarily attributed to changes in the thickness of Cr_2O_3.

Table 5 displays the ASR before and after steam oxidation, as determined by volumetric segmentation and weight gain analysis, along with the corresponding measured values. The threshold for the metal support was set at 5×10^{-3} Ωcm^2, as contributions below this level are considered minor. After 650 h of steam oxidation, the ASR remained below this threshold, confirming minimal impact on cell performance. Compared to weight gain analysis, the ASR derived from segmentation-based thickness changes more closely aligns with the measured values, particularly after steam oxidation. We attributed the observed weight gain to variations in the thickness of Cr_2O_3. In actual samples, FeO_x may form within the alloy, and subtracting its contribution yields a thickness closer to the measured values.

Thus, the structures and oxide scale thicknesses of porous stainless steel with complex geometries were quantified using deep learning models. The resulting shape parameters and conductivity values were subsequently used to model ASR, confirming negligible performance degradation after 650 h. Although previous studies attributed resistance increases to tortuosity within the porous body [61], the present results suggest that surface growth of Cr_2O_3, arising from minor thickness increases, is the primary contributing factor. This observation is consistent with resistance increases induced by oxidation within interconnects [62].

Table 5
Comparison of evaluated and calculated ASR before and after steam oxidation at 600 °C under 50% H_2–50% H_2O exposure for 650 h.

	Area specific resistance [x10^{-3}Ωcm^2]	
	0 h	650 h
Experiment	1.76	2.24
Volumetric segmentation	2.15	2.94
Weight gain	2.07	3.16

3.2.3. Prediction of ASR in the metal support under humidified hydrogen atmosphere

Our discussion in Section 3.2.2 revealed that an increase in Cr_2O_3 thickness, as quantified by a deep learning model, correlates with a rise in the ASR of porous stainless steel. In this section, we extend this analysis by predicting the ASR during prolonged oxidation. The oxidation behavior of porous stainless steel is assumed to follow Wagner's law. Accordingly, the thickness of Cr_2O_3 (L) is derived from the oxidation-induced weight gain (Δm) as described by Wagner's law in Equation (9) [61].

$$L = \frac{\sqrt{k_p t}}{\rho \theta}, \tag{9}$$

where k_p is the parabolic rate constant, t is the exposure time in the oxidizing environment, ρ is the density of Cr_2O_3, and θ is the oxygen weight fraction in Cr_2O_3. The k_p value, calculated from the weight gain data in Fig. 4, is 2.07×10^{-14} g^{2}cm^{-4}s^{-1}. This calculation employs the surface area obtained through BET measurements.

In this prediction, the Cr_2O_3 region segmented after 650 h (Section 3.2.2) was thickened according to Wagner's law, while the alloy phase was proportionally reduced. The resulting microstructure was then simulated using GeoDict. Based on these simulated microstructures at 4400 and 8400 h, the ASRs were calculated using the equivalent circuit shown in Fig. 6. Fig. 7 displays the simulated structures at 650, 4400, and 8400 h, along with the average Cr_2O_3 thickness and the corresponding ASRs. The oxide layer thickness increased from 1.2 μm at 650 h to 2.9 μm at 8400 h. Consequently, alloy regions composed of smaller particles became fully enveloped by the oxide scale, leading to their isolation and the interruption of electron conduction paths. However, simulation results for the porous structure revealed that although small particles became isolated, the ASR remained as low as 7.3 mΩcm^2 even after 8400 h, suggesting a negligible impact on cell performance. This outcome is attributed to the considerably higher electronic conductivity of stainless steel relative to those of the Mn–Cr spinel oxide and Cr_2O_3; as long as some electron conduction paths remain, the increase in resistance is minimal.

Notably, under practical operating conditions, Cr depletion may occur in porous stainless steel. Fig. 8 presents the sample SEM cross-

Table 4
Thickness and conductivity of each resistance component used in the equivalent circuit model.

Resistance	Material	Method	Thickness [μm]	Conductivity [S cm^{-1}]	ASR [x10^{-3} Ω cm^2]
R1	Mn–Cr spinel	TEM–EDS	0.44	1.15×10^{-1} [58]	0.384
R2	Cr_2O_3	Image segmentation and thickness analysis	0.51 (before) 0.80 (after)	7.43×10^{-2} [37]	0.687 (before) 1.077 (after)
		Weight gain	0.48 (before) 0.88 (after)		0.646 (before) 1.185 (after)
R3	1C44Mo29	Segmentation and conductivity calculation	250	2.68×10^3	9.34×10^{-3} (before) 1.74×10^{-2} (after)
R4	Cr_2O_3	Image segmentation and thickness analysis	0.51 (before) 0.80 (after)	7.43×10^{-2} [37]	0.687 (before) 1.077 (after)
		Weight gain	0.48 (before) 0.88 (after)		0.646 (before) 1.185 (after)
R5	Mn–Cr spinel	TEM–EDS	0.44	1.15×10^{-1} [58]	0.384

	650 h (evaluated)	4400 h (simulated)	8400 h (simulated)
Porous structure after steam oxidation	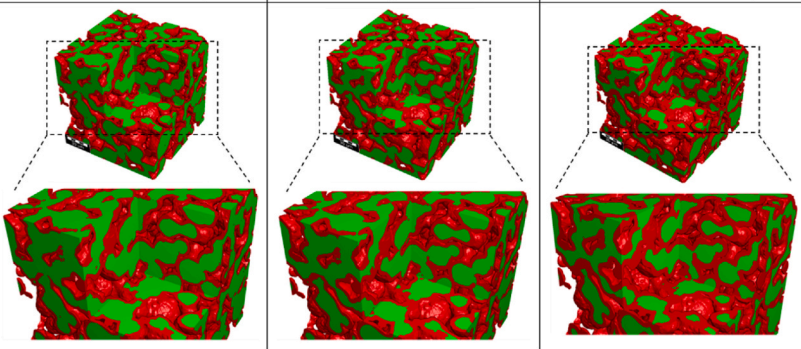		
Oxide scale thickness [μm]	1.2	2.2	2.9
ASR [mΩcm² at 600 °C]	3.1	5.6	7.3

Fig. 7. Predicted porous structure, oxide scale thickness, and ASR after 4400 and 8400 h at 600 °C under 50% H_2–50% H_2O.

(a)

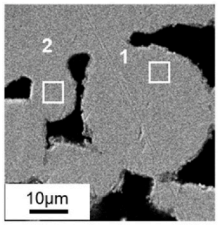

(b)

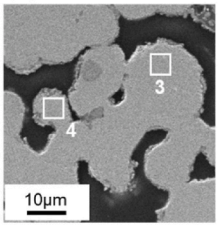

(c)

Region	Cr content [mass%]
1	17.0
2	15.6
3	15.5
4	13.2

Fig. 8. Cross-sectional images (a) before and (b) after steam oxidation at 600 °C under 50% H_2–50% H_2O for 650 h. (c) Cr content in selected regions based on EDS measurements.

section and quantitative EDS results of Cr content before steam oxidation (equivalent to the condition after pre-oxidation at 800 °C for 10 h) and after steam oxidation at 600 °C under 50% H_2/50% H_2O for 650 h. Compared to the composition listed in Table 1, the Cr content decreases from 17.0% after pre-oxidation to 15.6% after steam oxidation. Moreover, smaller particles in each sample tend to exhibit a greater decrease in Cr content. Pre-oxidation causes Cr evaporation under atmospheric conditions [25], whereas steam oxidation consumes Cr through the formation of Cr_2O_3. Cr depletion promotes breakaway oxidation, which can lead to detrimental effects such as reduced mechanical strength and pore closure. This may represent the degradation mechanism associated with long-term oxidation of metal supports. For powder-metallurgy-based MS-SOFCs, quantitative evaluation of Cr consumption during both pre-oxidation and steam oxidation, along with lifetime prediction accounting for Cr depletion, is essential in future research.

Oxidation of stainless steel is suppressed under low-temperature, low-humidity conditions [63]. Optimizing pre-oxidation parameters to apply lower temperatures and shorter holding times can suppress Cr evaporation [25]. Increasing the particle size of stainless steel to expand the Cr reservoir is also beneficial. According to Huczkowski et al. [64], oxidation proceeds more rapidly in porous stainless steel owing to its large surface area and thin effective thickness. Therefore, enlarging particle size can mitigate both Cr depletion and accelerated oxidation under humidified atmospheres. Furthermore, coating technologies such as electrophoretic deposition [65] and atomic layer deposition [27] are effective in suppressing oxidation. Optimizing these approaches is expected to mitigate degradation caused by Cr mobility and enhance long-term durability.

In this section, it is demonstrated that the oxidation of the porous stainless steel support contributes only a negligible 7.3 mΩcm^2 to the overall resistance after 8400 h. This model is useful for predicting microstructural changes after long-term operation with the segmented three-dimensional structure of the porous stainless steel and the oxidation rate constant from short-term oxidation tests. It should help to consider the properties of stainless alloy particles and adjusting sintering conditions. By configuring the trigger for breakaway oxidation in this model as the ratio of oxide scale thickness to alloy particle diameter, it will become possible to predict the lifetime of degradation caused by Cr depletion. This, in turn, will enable long term prediction of the changes in the ohmic resistance of the interface between bonding layer and anode scaffold. We believe these methods for predicting the future structure of porous stainless steel will greatly advance research on MS-SOCs.

4. Conclusions

This study examined the long-term degradation mechanism of MS-SOFCs employing porous stainless steel fabricated via tape casting. A degradation rate of 5.2% per 1000 h was observed over 8400 h of testing at 600 °C under 78% H_2–16% N_2–6% H_2O. Oxide scale growth or breakaway oxidation occurred in small stainless-steel particles within the anode bonding layer, as Cr diffused into ScYSZ, depleting the Cr content and increasing ohmic resistance between the anode scaffold and bonding layer. Following the durability test, a reaction between Ni catalyst particles and Cr in the anode layer was observed, resulting in decreased activity of the hydrogen oxidation reaction. To examine the relationship between morphological changes caused by oxidation under humidified hydrogen and electrical resistance, 3D images acquired by plasma FIB-SEM were processed using 3D U-Net, a deep learning model, for volumetric phase segmentation. An equivalent circuit model was developed to evaluate the ASR contributions of the Mn–Cr spinel oxide,

Cr_2O_3, and porous alloy layers that comprise the coating. Increases in Cr_2O_3 thickness due to steam oxidation contributed more substantially to resistance than changes in the 3D structure. Using the parabolic oxidation rate constant derived from weight gain measurements, a predictive model was constructed to simulate oxide scale thickening on the porous stainless steel surface. Even after 8400 h of oxidation under 50% H_2–50% H_2O, the impact on cell performance remained minimal, as the ASR of the porous stainless steel was only 7.3 $m\Omega cm^2$; however, the results suggested that Cr depletion may occur during long-term steam oxidation. Thus, in MS-SOFCs based on porous stainless steel, the dominant degradation factors are activity loss due to Cr poisoning in the anode, increased Cr_2O_3 accumulation at the anode/metal support interface, and breakaway oxidation of the porous metal support under highly humidified conditions. Durability can be further improved by optimizing the pre-oxidation process and the particle size of stainless steel. In conclusion, this work highlights the critical importance of addressing Cr-related degradation mechanisms and optimizing processing conditions to extend the operational lifetime of MS-SOFCs, thereby advancing their practical application in sustainable energy systems.

CRediT authorship contribution statement

Yohei Miura: Writing – review & editing, Writing – original draft, Visualization, Validation, Software, Project administration, Methodology, Investigation, Formal analysis, Data curation, Conceptualization. **Satoshi Takemiya:** Investigation, Formal analysis, Data curation. **Yuuki Shibata:** Investigation, Formal analysis, Data curation. **Yuki Cho:** Investigation, Formal analysis, Data curation. **Kosuke Hara:** Investigation. **Takeshi Shiomi:** Writing – review & editing, Writing – original draft, Supervision, Funding acquisition. **Gen Inoue:** Writing – review & editing, Supervision, Conceptualization. **Prabhakar Singh:** Writing – review & editing, Supervision. **Shunsuke Taniguchi:** Writing – review & editing, Writing – original draft, Supervision, Resources, Project administration. **Kazunari Sasaki:** Writing – review & editing, Supervision.

Declaration of competing interest

The authors declare that they have no known competing financial interests or personal relationships that could have appeared to influence the work reported in this paper.

Acknowledgments

The authors are grateful to the New Energy and Industrial Technology Development Organization (NEDO) for commissioning the project JPNP20003. We appreciate Yasuko Kitahara and Tomoaki Aoki from JFE Techno-Research Corporation for investigating the steam oxidation of porous stainless steel with STEM–EDS, and we thank Akiyo Yoshida in Toray Research Center for conducting the plasma FIB-SEM. Additionally, we would also like to thank Isao Yamashita and Shihomi Okabe from the Sumika Chemical Analysis Service for FE-SEM and STEM–EDS analysis.

Appendix A. Supplementary data

Supplementary data to this article can be found online at https://doi.org/10.1016/j.jpowsour.2026.240130.

Data availability

The data that has been used is confidential.

References

[1] S. Pirou, B. Talic, K. Brodersen, T.L. Skafte, A. Hauch, J.V.T. Høgh, H. Henriksen, Å. H. Persson, A. Hagen, Durability enhancement of novel monolithic metal supported solid oxide fuel cells through processing optimizations, Int. J. Hydrogen Energy 48 (2023) 11017–11028, https://doi.org/10.1016/j.ijhydene.2022.12.139.

[2] S. Pirou, B. Talic, K. Brodersen, A. Hauch, H.L. Frandsen, T.L. Skafte, Å. H Persson, J. Vt Høgh, H. Henriksen, M. Navasa, X.-Y. Miao, X. Georgolamprou, S.P. V. Foghmoes, P.V. Hendriksen, E.R. Nielsen, J. Nielsen, A. C Wulff, S. H Jensen, P. Zielke, A. Hagen, Production of a monolithic fuel cell stack with high power density, Nat. Commun. 13 (1) (2022) 1–8, https://doi.org/10.1038/s41467-022-28970-w.

[3] Y. Miura, S. Takemiya, Y. Fukuyama, T. Kato, S. Taniguchi, K. Sasaki, Improvement of the internal reforming of metal-supported SOFC at low temperatures, Int. J. Hydrogen Energy 48 (65) (2023) 25487–25498, https://doi.org/10.1016/j.ijhydene.2023.03.195.

[4] R. Leah, A. Bone, M. Lankin, A. Selcuk, M. Rahman, A. Clare, L. Rees, S. Phillip, S. Mukerjee, M. Selby, Ceres power steel cell technology: rapid progress towards a truly commercially viable SOFC, ECS Trans. 68 (2015) 95–107, https://doi.org/10.1149/06801.0095ecst.

[5] E. Dogdibegovic, R. Wang, G.Y. Lau, A. Karimaghaloo, M.H. Lee, M.C. Tucker, Progress in durability of metal-supported solid oxide fuel cells with infiltrated electrodes, J. Power Sources 437 (2019) 226935, https://doi.org/10.1016/j.jpowsour.2019.226935.

[6] F. Thaler, D. Udomsilp, W. Schafbauer, C. Bischof, Y. Fukuyama, Y. Miura, M. Kawabuchi, S. Taniguchi, S. Takemiya, A. Nenning, A.K. Opitz, M. Bram, Redox stability of metal-supported fuel cells with nickel/gadolinium-doped ceria anode, J. Power Sources 434 (2019) 226751, https://doi.org/10.1016/j.jpowsour.2019.226751.

[7] M.C. Tucker, Dynamic-temperature operation of metal-supported solid oxide fuel cells, J. Power Sources 395 (2018) 314–317, https://doi.org/10.1016/j.jpowsour.2018.05.094.

[8] Nissan Unveils World's First solid-oxide Fuel Cell Vehicle, 2016. https://global.nissannews.com/en/releases/160614-01-e.

[9] J.J. Botti, M.J. Grieve, J.A. MacBain "Electric Vehicle Range Extension Using an SOFC APU" SAE technical paper 2005-01-1172, World Congress & Exhibition (SAE International)..

[10] V. Lawlor, M. Reissig, J. Makinson, J. Rechberger, SOFC system for battery electric vehicle range extension: results of the first half of the Mestrex Project, ECS Trans. 78 (2017) 191–195, https://doi.org/10.1149/07801.0191ecst.

[11] X.-D. Zhou, University of Louisiana at Lafayette "High performance metal-supported SOFC system for range extension of commercial aviation". ASCEND and REEACH Programs Kickoff Meeting, 2021.

[12] H. Sumi, S. Nakabayashi, T. Kawada, Y. Uchiyama, N. Uchiyama, K. Ichihara, Demonstration of SOFC power sources for drones (UAVs; unmanned aerial vehicles), ECS Trans. 91 (2019) 149–157, https://doi.org/10.1149/09101.0149ecst.

[13] Z. Zhu, B. Hu, M.C. Tucker, Dynamic operation of metal-supported solid oxide electrolysis cells, Int. J. Hydrogen Energy 59 (2024) 316–321, https://doi.org/10.1016/j.ijhydene.2024.01.345.

[14] A. Hagen, R. Caldogno, F. Capotondo, X. Sun, Metal supported electrolysis cells, Energies 15 (2022), https://doi.org/10.3390/en15062045.

[15] A. Hagen, D. Tasca, A.D. Faria, F. Capotondo, R. Caldogno, B.R. Sudireddy, X. Sun, Reversible operation of metal supported solid oxide cells, J. Electrochem. Soc. 171 (2024) 044505, https://doi.org/10.1149/1945-7111/ad3aaa.

[16] J. Mao, E. Wang, H. Wang, M. Ouyang, Y. Chen, H. Hu, L. Lu, D. Ren, Y. Liu, Progress in metal corrosion mechanism and protective coating technology for interconnect and metal support of solid oxide cells, Renew. Sustain. Energy Rev. 185 (2023) 113597, https://doi.org/10.1016/j.rser.2023.113597.

[17] H. Hooshyar, T. Jonsson, J. Hall, J.-E. Svensson, L.G. Johansson, J. Liske, "The Effect of H2 and H2O on the Oxidation of 304LStainless Steel at 600 ∘C: general Behaviour (Part I)" oxid, Metals 85 (2016) 321–342, https://doi.org/10.1007/s11085-015-9597-5.

[18] M. Palcut, L. Mikkelsen, K. Neufeld, M. Chen, R. Knibbe, P.V. Hendriksen, Corrosion stability of ferritic stainless steels for solid oxide electrolyser cell interconnects, Corros. Sci. 52 (2010) 3309–3320, https://doi.org/10.1016/j.corsci.2010.06.006.

[19] Y. Zhou, T. Chen, J. Li, C. Yuan, X. Xin, G. Chen, G. Miao, W. Zhan, Z. Zhan, S. Wang, Long-term stability of metal-supported solid oxide fuel cells employing infiltrated electrodes, J. Power Sources 295 (2015) 67–73, https://doi.org/10.1016/j.jpowsour.2015.06.114.

[20] P. Blennow, J. Hjelm, T. Klemensø, Å. Persson, K. Brodersen, A.K. Srivastava, H. L. Frandsen, M. Lundberg, S. Ramousse, M. Mogensen, Development of planar metal supported SOFC with novel cermet anode, ECS Trans. 25 (2009) 701–710, https://doi.org/10.1149/1.3205585.

[21] A. Hagen, A.C. Wulff, P. Zielke, X. Sun, B. Talic, I. Ritucci, H.L. Frandsen, S. H. Jensen, W.R. Kiebach, P.V. Hendriksen, SOFC stacks for mobile applications with excellent robustness towards thermal stresses, Int. J. Hydrogen Energy 45 (2020) 29201–29211, https://doi.org/10.1016/j.ijhydene.2020.07.159.

[22] A. Hagen, X. Sun, B.R. Sudireddy, Å. Persson, Metal supported SOFCs for Mobile applications using hydrocarbon fuels, J. Electrochem. Soc. 167 (2020) 104510, https://doi.org/10.1149/1945-7111/ab9b9d.

[23] S.-L. Zhang, C.-X. Li, C.-J. Li, M. Liu, G.-J. Yang, Investigation into the diffusion and oxidation behavior of the interface between a plasma-sprayed anode and a porous steel support for solid oxide fuel cells, J. Power Sources 323 (2016) 1–7, https://doi.org/10.1016/j.jpowsour.2016.05.020.

[24] G. Reiss, H.L. Frandsen, A.H. Persson, C. Weiß, W. Brandstätter, Numerical evaluation of oxide growth in metallic support microstructures of solid oxide fuel cells and its influence on mass transport, J. Power Sources 297 (2015) 388–399, https://doi.org/10.1016/j.jpowsour.2015.08.020.
[25] D. Koszelow, M. Makowska, F. Marone, G. Cempura, M. Tomas, J. Froitzheim, S. Molin, Pre-oxidation of porous ferritic Fe22Cr alloys for lifespan extension at high-temperature, Corros. Sci. 234 (2024) 112129, https://doi.org/10.1016/j.corsci.2024.112129.
[26] M. Reisert, V. Berova, A. Aphale, P. Singh, M.C. Tucker, Oxidation of porous stainless steel supports for metal-supported solid oxide fuel cells, Int. J. Hydrogen Energy 45 (55) (2020) 30882–30897, https://doi.org/10.1016/j.ijhydene.2020.08.015.
[27] F. Shen, M.M. Welander, M.C. Tucker, Oxidation of porous stainless steel supports for metal-supported solid oxide electrolysis cells, Int. J. Hydrogen Energy 48 (2023) 12168–12175, https://doi.org/10.1016/j.ijhydene.2022.11.235.
[28] E. Stefan, C. Denonville, Y. Larring, M. Stange, R. Haugsrud, "Oxidation study of porous metal substrates for metal supported proton ceramic electrolyzer cells" corros, Sci. 164 (2020) 108335, https://doi.org/10.1016/j.corsci.2019.108335.
[29] E. Sarasketa-Zabala, L. Otaegi, L.M. Rodriguez-Martinez, M.A. Alvarez, N. Burgos, F. Castro, I. Villarreal, High temperature stability of porous metal substrates under highly humidified hydrogen conditions for metal supported Solid Oxide Fuel Cells, Solid State Ionics (2012) 222–223, https://doi.org/10.1016/j.ssi.2012.06.014.
[30] K. Xu, Z. Chen, C. Bao, W. Yan, W. Tang, K. Xu, W. Guan, G. Li, Y. Chen, L. Zhu, Unravelling the oxidation behaviors of porous stainless steel 430L substrate for metal-supported solid oxide fuel cells, Int. J. Hydrogen Energy 73 (2024) 577–589, https://doi.org/10.1016/j.ijhydene.2024.06.092.
[31] S.H. Ibrahim, D. Koszelow, M. Makowska, S. Molin, Modeling of microstructure evolution during high-temperature oxidation of porous Fe-Cr steels, Mater. Des. 249 (2025) 113536, https://doi.org/10.1016/j.matdes.2024.113536.
[32] H. Hwang, S.M. Choi, J. Oh, S.-M. Bae, J.-H. Lee, J.-P. Ahn, J.-O. Lee, K.-S. An, Y. Yoon, J.-H. Hwang, Integrated application of semantic segmentation-assisted deep learning to quantitative multi-phased microstructural analysis in composite materials: case study of cathode composite materials of solid oxide fuel cells, J. Power Sources 471 (2020) 228458, https://doi.org/10.1016/j.jpowsour.2020.228458.
[33] A. Sciazko, Y. Komatsu, A. Nakamura, Z. Ouyang, T. Hara, N. Shikazono, 3D microstructures of solid oxide fuel cell Ni-YSZ anodes with carbon deposition, Chem. Eng. J. 460 (2023) 141680, https://doi.org/10.1016/j.cej.2023.141680.
[34] R. Yamagishi, A. Sciazko, Z. Ouyang, Y. Komatsu, K. Nishimura, Naoki Shikazono, Super-resolved In-operando observation of SOFC pattern electrodes, ECS Trans. 103 (1) (2021) 2087–2098, https://doi.org/10.1149/10301.2087ecst.
[35] D. Udomsilp, J. Rechberger, R. Neubauer, C. Bischof, F. Thaler, W. Schafbauer, N. H. Menzler, L.G.J. de Haart, A. Nenning, A.K. Opitz, O. Guillon, M. Bram, "Metal-supported solid oxide fuel cells with exceptionally high power density for range extender systems" cell Rep, Phys. Sci. 1 (2020) 100072, https://doi.org/10.1016/j.xcrp.2020.100072.
[36] R. Caldogno, J.Z. Garcia, X. Sun, A. Hagen, Electrochemical characterisation and durability assessment of Ni/GDC-infiltrated metal-supported solid oxide cells for co-electrolysis operation, J. Power Sources 665 (2026) 239016.
[37] A. Holt, P. Kofstad, Electrical conductivity and defect structure of Cr2O3. II. Reduced temperatures (<~ 1000 C), Solid State Ionics 69 (1994) 137–143, https://doi.org/10.1016/0167-2738(94)90402-2.
[38] B.M. Warnes, F.F. Aplan, G. Simkovich, Electrical conductivity and seebeck voltage of Fe2O3, pure and doped, as a function of temperature and oxygen pressure, Solid State Ionics 12 (1984) 271–276, https://doi.org/10.1016/0167-2738(84)90156-5.
[39] D.-S. Lee, W.S. Kim, S.H. Choi, J. Kim, H.-W. Lee, J.-H. Lee, Characterization of ZrO_2 co-doped with Sc_2O_3 and CeO_2 electrolyte for the application of intermediate temperature SOFCs, Solid State Ionics 176 (2005) 33–39, https://doi.org/10.1016/j.ssi.2004.07.013.
[40] J.P. Souza, T.G. Fujimoto, R.M. Batista, M.C. Steil, R. Muccillo, E.N.S. Muccillo, Phase transformation/stabilization and ionic conductivity in tantalum oxide co-doped zirconia-scandia solid electrolyte, Ionics 28 (2022) 3919–3926, https://doi.org/10.1007/s11581-022-04604-5.
[41] S. Omar, W.B. Najib, W. Chen, N. Bonanos, Electrical Conductivity of 10 mol% Sc2O3–1 mol% M2O3–ZrO2 Ceramics, J. Am. Ceram. Soc. 95 (6) (2012) 1965–1972, https://doi.org/10.1111/j.1551-2916.2012.05126.x.
[42] M. Kubicek, A. Limbeck, T. Frömling, H. Hutter, J. Fleig, Relationship between cation segregation and the electrochemical oxygen reduction kinetics of La0. 6Sr0. 4CoO3− δ thin film electrodes, J. Electrochem. Soc. 158 (6) (2011) B727, https://doi.org/10.1149/1.3581114.
[43] Y. Ishibashi, K. Matsumoto, S. Futamura, Y. Tachikawa, J. Matsuda, S.M. Lyth, Y. Shiratori, S. Taniguchi, K. Sasaki, Improved redox cycling durability in alternative Ni alloy-based SOFC anodes, J. Electrochem. Soc. 167 (2020) 124517, https://doi.org/10.1149/1945-7111/abac87.
[44] X. Zhou, N. Yan, K.T. Chuang, J. Luo, Progress in La-doped SrTiO3 (LST)-based anode materials for solid oxide fuel cells, RSC Adv. 4 (1) (2014) 118–131, https://doi.org/10.1039/C3RA42666A.
[45] B.B. Ebbinghaus, Thermodynamics of gas phase chromium species: the chromium oxides, the chromium oxyhydroxides, and volatility calculations in waste incineration processes, Combust. Flame 93 (1993) 119–137, https://doi.org/10.1016/0010-2180(93)90087-J.
[46] M. Brandner, M. Bram, J. Froitzheim, H.P. Buchkremer, D. Stöver, Electrically conductive diffusion barrier layers for metal-supported SOFC, Solid State Ionics 179 (27–32) (2008) 1501–1504, https://doi.org/10.1016/j.ssi.2008.03.002.
[47] P. Blennow, T. Klemensø, Å.H. Persson, K. Brodersen, A.K. Srivastava, B. R. Sudireddy, S. Ramousse, M. Mogensen, Metal-supported SOFC with ceramic-based anode, ECS Trans. 35 (1) (2011) 683–692, https://doi.org/10.1149/1.3570047.
[48] B.J. McKenna, N. Christiansen, R. Schauperl, P. Prenninger, J. Nielsen, P. Blennow, T. Klemensø, S. Ramousse, A. Kromp, A. Weber, Advances in metal supported cells in the METSOFC EU consortium, Fuel cells 13 (4) (2013) 592–597, https://doi.org/10.1002/fuce.201200185.
[49] R. Caldogno, I. Giaccardo, X. Sun, A. Hagen, Green syngas production with metal-supported solid oxide cells, J. Power Sources 654 (2025) 237825, https://doi.org/10.1016/j.jpowsour.2025.237825.
[50] F. Capotondo, M.C. Tucker, B.R. Sudireddy, A. Hagen, Infiltrated electrodes for metal supported solid oxide electrolysis cells, J. Power Sources 646 (2025) 237296, https://doi.org/10.1016/j.jpowsour.2025.237296.
[51] M.P. Hoerlein, M. Riegraf, R. Costa, G. Schiller, K.A. Friedrich, A parameter study of solid oxide electrolysis cell degradation: microstructural changes of the fuel electrode, Electrochim. Acta 276 (2018) 162–175, https://doi.org/10.1016/j.electacta.2018.04.170.
[52] D. Koszelow, M. Makowska, A. Drewniak, G. Cempura, P. Jasiński, S. Molin, High-temperature corrosion of ~ 30 pct porous FeCr stainless steels in air: Long-Term evaluation up to breakaway, Metall. Mater. Trans. A 54 (6) (2023) 2244–2258, https://doi.org/10.1007/s11661-023-07005-z.
[53] Math2Market, Segmentation methods for FIB-SEM images of Li+ - cathodes. https://www.math2market.com/geodict-aplications/segmentation-methods-for-fib-sem-images-of-li-ion-cathodes.html.
[54] Ö. Çiçek, A. Abdulkadir, S. S. Lienkamp, T. Brox, and O. Ronneberger, "3D U-Net: learning dense volumetric segmentation from sparse annotation", Medical Image Computing and Computer-Assisted Intervention–MICCAI 2016: 19Th International Conference, Athens, Greece, October 17-21, 2016, Proceedings, Part II 19 (pp. 424-432). Springer International Publishing.https://doi.org/10.1007/978-3-319-46723-8_49.
[55] A.A. Taha, A. Hanbury, Metrics for evaluating 3D medical image segmentation: analysis, selection, and tool, BMC Med. Imaging 15 (2015) 1–28, https://doi.org/10.1186/s12880-015-0068-x.
[56] O. Ronneberger, P. Fischer and T. Brox, "U-net: convolutional networks for biomedical image segmentation" medical image computing and computer-assisted intervention–MICCAI 2015: 18Th International Conference, Munich, Germany, October 5-9, 2015, Proceedings, Part III 18 (pp. 234-241). Springer international publishing.https://doi.org/10.1007/978-3-319-24574-4_28.
[57] S. Müller, C. Sauter, R. Shunmugasundaram, N. Wenzler, V. De Andrade, F. De Carlo, E. Konukoglu, V. Wood, Deep learning-based segmentation of lithium-ion battery microstructures enhanced by artificially generated electrodes, Nat. Commun. 12 (1) (2021) 6205, https://doi.org/10.1038/s41467-021-26480-9.
[58] Springer Materials, "MnCr2O4 (Cr2Mno4) Crystal Structure"https://materials.springer.com/isp/crystallographic/docs/sd_0553605.
[59] Springer Materials, "Cr2O3 Crystal Structure"https://materials.springer.com/isp/crystallographic/docs/sd_0541813.
[60] Z. Lu, J. Zhu, E.A. Payzant, M.P. Paranthaman, Electrical conductivity of the manganese chromite spinel solid solution, J. Am. Ceram. Soc. 88 (4) (2005) 1050–1053, https://doi.org/10.1111/j.1551-2916.2005.00205.x.
[61] Z. Zhou, V.K. Nadimpalli, D.B. Pedersen, V. Esposito, Degradation mechanisms of metal-supported solid oxide cells and countermeasures: a review, Materials 14 (2021) 3139, https://doi.org/10.3390/ma14113139.
[62] T. Brylewski, S. Molin, M. Stygar, M. Bik, P. Jeleń, M. Sitarz, A. Gil, M. Chen, P. V. Hendriksen, Oxidation kinetics and electrical properties of oxide scales formed under exposure to air and Ar–H2-H2O atmospheres on the Crofer 22 H ferritic steel for high-temperature applications such as interconnects in solid oxide cell stacks, Int. J. Hydrogen Energy 94 (2024) 209–222, https://doi.org/10.1016/j.ijhydene.2024.11.091.
[63] Y. Inoue, S. Taniguchi, C. Uryu, H.-C. Pham, J.-T. Chou, K. Sasaki, Steam oxidation behavior of four general-purpose stainless steels in humidified hydrogen environment of solid oxide fuel cell, J. Electrochem. Soc. 172 (2025) 044503, https://doi.org/10.1149/1945-7111/adc5a7.
[64] P. Huczkowski, V. Shemet, J. Piron-Abellan, L. Singheiser, W.J. Quadakkers, Oxidation limited lifetimes of chromia forming ferritic steels, Mater. Corros. 55 (11) (2004) 825–830, https://doi.org/10.1115/1.1782925.
[65] Z. Zhu, C.D. Uzu, U. Pal, S. Gopalan, A.M. Hussain, N. Dale, Y. Fukuyama, Y. Miura, Y. Miyoshi, S. Basu, Comparison of Cu–Mn and Mn–Co spinel coatings for solid oxide fuel cell interconnects, Int. J. Hydrogen Energy 47 (2022) 36953–36963, https://doi.org/10.1016/j.ijhydene.2022.08.239.